JOURNAL OF THERMOPHYSICS AND HEAT TRANSFER
Vol. 17, No. 3, July–September 2003

Surface Heat Transfer Measurements Inside a Supersonic Combustor by Laser-Induced Fluorescence

K. Kontis*
University of Manchester, Manchester, England M60 1QD, United Kingdom

A study has been conducted to measure surface temperatures inside a model rectangular supersonic combustor by the use of a nonintrusive thermal imaging system, based on the fluorescence properties of a dysprosium doped yttrium–aluminum–garnet (Dy^{3+}:YAG) thermographic phosphor. In this system, the phosphor coating on the test surface is excited by a pulsed Nd:YAG laser. The resulting fluorescent emission of the temperature-sensitive 456-nm transition and that of the temperature-independent 496-nm transition are acquired by the use of a pair of image-intensified charge-coupled device cameras. The ratio of the acquired emissions is then correlated to temperature. The wind tunnel was a blowdown type that used vitiated air with nominal conditions at the entrance of the test section: $M_\infty = 2.5$, $P_o = 5 \times 10^5$ N/m^2, $T_o = 800$ K, and $Re_\infty/\text{m} = 9.6 \times 10^6$. The fuel was hydrogen gas at room temperature, injected parallel to the tunnel through a fuel-injector slit located along the backward surface of a step. The results under hot flow conditions were compared with numerical simulations performed using a two-dimensional Navier–Stokes code with full chemistry. Temperature measurements demonstrate the feasibility of laser-induced fluorescence for surface heat transfer studies in reactive flows involving significant unsteadiness and transient phenomena.

Nomenclature

A	=	preexponential factor for Arrhenius law
c_p	=	pressure specific heat, Jkg^{-1} K^{-1}
D_{im}	=	molecular diffusion coefficient of ith species, m^{2}s^{-1}
D_{it}	=	turbulent diffusion coefficient of ith species, m^{2}s^{-1}
E	=	total energy or Arrhenius activation energy, cal mole^{-1}
h	=	height of backward facing step, m
h_i	=	specific enthalpy of ith species, Jkg^{-1}
L	=	coating thickness, m
M	=	Mach number
$\dot{m}_i$	=	mass flux of i species, kgs^{-1}
n	=	temperature exponent for Arrhenius law
NS	=	number of species
P	=	pressure, Nm^{-2}
q	=	heat flux, Wm^{-2}
R	=	universal gas constant, Jkg^{-1} mole^{-1} K^{-1}
Re	=	Reynolds number
s	=	specific entropy, Jkg^{-1}K^{-1}
T	=	temperature, K
t	=	time, s
u	=	horizontal component of velocity, ms^{-1}
v	=	vertical component of velocity, ms^{-1}
W_i	=	molecular weight of ith species, kg kmole^{-1}
x	=	horizontal direction, m
Y_i	=	mass fraction of ith species
y	=	vertical direction, m
y^*	=	semi-infinity penetration depth, m
α	=	thermal diffusivity, m^{2}s^{-1}
η	=	transformed coordinate in vertical direction
κ	=	thermal conductivity, Wm^{-1} K^{-1}
μ	=	dynamic viscosity, kg m^{-1}s^{-1}
ξ	=	transformed coordinate in horizontal direction
ρ	=	density, kg m^{-3}
σ	=	normal stress, Nm^{-2}
τ	=	shear stress, Nm^{-2}
$\dot{\omega}_i$	=	rate of production of ith species during chemical reaction, mole m^{-3} s^{-1}

Subscripts

i	=	ith species
ini	=	initial
ℓ	=	laminar
o	=	total condition
sub	=	substrate
t	=	turbulent
TSP	=	temperature sensitive paint
w	=	wall
x	=	horizontal direction
xy	=	reference plane
y	=	vertical direction
yx	=	reference plane
∞	=	infinity

Presented as Paper 2002-3105 at the AIAA/ASME 8th Joint Thermophysics and Heat Transfer Conference, St. Louis, MO; 24–26 June 2002; received 6 September 2002; revision received 24 January 2003; accepted for publication 26 January 2003.

*Lecturer of Aerospace Engineering, Department of Mechanical, Aerospace, and Manufacturing Engineering, Division of Thermofluids, Institute of Science and Technology, P.O. Box 88; k.kontis@umist.ac.uk. Member AIAA.

Introduction

CURRENT interest in supersonic combustion has initiated many research studies to understand the flowfield and predict the performance of supersonic combustors.[1,2] Because of the inherent difficulties of the experimental setup and measurements, the majority of the experiments have been done under cold flow conditions (without combustion).[3,4] Those experiments provided the fundamental understanding of the mixing mechanism and load distribution in supersonic and hypersonic flows. Experiments in hot flow (with combustion) have been directed toward measuring pressure distributions along the internal surfaces, concentration of chemical species, and engine thrust.[5,6] These results have indicated drastic changes of the fuel and main flow properties, which are due mainly to the shock wave system located upstream of the combustion region (precombustion shock wave system).

The present study aims to measure experimentally the surface temperatures inside a model supersonic combustor on the fuel injection side, by the use of a nonintrusive, high spatial and temporal resolution thermal imaging system, based on the fluorescence

properties of dysprosium, doped at 3%, into an yttrium–aluminum–garnet (Dy^{3+}:YAG) thermographic phosphor.[7] The results under hot flow conditions will be compared with numerical simulations.

Laser-Induced Fluorescence Technique

Of the available optical diagnostic techniques, laser-induced fluorescence (LIF) was considered to be the most effective diagnostic method for surface high-temperature measurements.[7] The primary components of the LIF thermal imaging system are 1) the neodymium doped yttrium–aluminum–garnet (Nd:YAG) pulsed laser, 2) a pair of image-intensified charge-coupled device (ICCD) cameras (Hamamatsu C5987), and 3) a diffraction grating polychromator (Jasco CT-50N). The arrangement with the polychromator was used in the initial studies[7] to analyze the entire emission spectrum of Dy:YAG and its dependence on temperature.

The emission analysis of Dy:YAG indicated that the phosphor starts to fluorescence 199.17 μs after being excited by the 355-nm tripled output of the Nd:YAG laser. The absorbed laser light excites the trivalent dysprosium to a high energy level, which radiatively and non radiatively decays to the F-level fluorescence, located at 496 nm (temperature independent). The G-level fluorescence, located at 456 nm, is temperature sensitive.[7] Therefore, F-level emission can be used as an internal standard for calibration of the G-level emission, which allows the temperature determination to be a relative measurement rather than an absolute intensity one. The fluorescence from the F and G levels disappears at a temperature of approximately 1800 K due to the large photon quenching rates. The lifetime of the F-level fluorescent emission is approximately 0.1 ms (Ref. 7).

The laser was allowed to operate at its optimum frequency of 10 Hz to minimize pulse-to-pulse energy deviations. Approximately 50 mJ of excitation energy over a beam diameter of 0.012 m were provided during each 5-ns laser pulse. Each pulse had an energy stability of 4% and a power drift of 6%. The timing and duration of the image-intensifier gate, or electronic shutter, on the ICCD cameras was precisely coordinated with the laser pulse by a pulse generator. It was adjusted to provide a 10-μs gate in a "single shot" mode of operation. This feature is very important at elevated temperatures, where the natural blackbody emission from the surface and the surroundings is high. The fluorescence signal from the test surface was collimated by an f-6 lens, was split into two equal paths by a cube beam splitter, and was then directed through two optical narrow band filters, at 496 and 456 nm for the F and G levels of fluorescence, respectively. The two paths were separately imaged on two ICCD cameras. To ensure that the images at the two wavelengths were spatially identical, matched imaging lenses were used. When the specified number of laser pulses comprising a single exposure were completed, the camera controller disabled the image-intensifier gate and stored the raw digital image data to a disk file for analysis. A high-performance personal computer provided the overall system control, as well as image storage and analysis.

Intensity differences over the test surface occur as a result of variations in the density of the phosphor coating, the laser excitation energy, and the energy level of the expanded laser beam output. For three-dimensional surfaces, variations in viewing angle due to surface curvature will affect the spatial emission intensities. Taking the ratio of the intensities of F and G levels can eliminate the influence of these factors. Before the collection of the fluorescent images for analysis, a pixel-to-pixel correspondence between the two images, projected onto the CCD cameras, was conducted. The spatial intensity response of the cameras was also established. Variations in the phosphor coating of the ICCD cameras' photocathode, which converts photons to electrons, caused differences in the pixel-to-pixel intensity values. Imaging a uniformly illuminated white surface checked the variation of the intensity response of the cameras. Obtaining a correction array for each image, focused on the detectors, eliminated the error. The array was established by the division of the individual pixel intensity by the average intensity of the image. The postacquisition analysis of the acquired images was performed using IPLab Spectrum (V.3.1.1 Signal Analytics Corporation) image and data analysis software. The ratio of the intensities of the F and G emissions was calculated for each pixel. It was then correlated to temperature. The calibration procedure is described in Ref. 7.

Because the LIF signal is very reproducible as a function of temperature, the accuracy of the technique corresponds to that of the thermocouple used for calibration,[7] which is in the range of ± 2.0 K, depending on the absolute temperature. The precision of the temperature is affected by a number of factors, like photon statistics, detector noise, and background signal levels. With the large signal levels from Dy:YAG crystals, the major limit to precision is the detector noise, which is 3%. The spatial resolution of the technique depends on the minimum pixel size, which can be resolved by the CCD camera. In the present study, it is equivalent to a square of side length 0.0001 m (or 0.1 mm). The temporal resolution depends on the choice of the data acquisition system. For example, a linear-array detector can offer a high sample rate in excess of 30 Hz. In the present study, a temporal resolution of less than 2 s can be achieved by setting the CCD camera in the maximum frequency acquisition mode. The time constant of the technique is of the order of 0.21 ms.

Apparatus and Procedure

The experiments were performed on a blowdown type design supersonic wind tunnel with vitiated air (Fig. 1). The nominal conditions at the entrance of the test section were $M_\infty = 2.5 \pm 2\%$, $P_o = 5 \times 10^5$ N/m^2, $T_o = 800$ K $\pm 3\%$, and $Re_\infty/\text{m} = 9.6 \times 10^6 \pm 5\%$. (The Reynolds number varies due to the variation in reservoir conditions.) The total run time of the tunnel was approximately 8 s with 4 s of steady-state flow conditions at nominal values. The complete synchronization of the valves for the air, hydrogen, and oxygen was achieved electronically, which allowed the valves to maintain a steady pressure inside the heater (typically within $\pm 3\%$). At the heater section, hydrogen gas and oxygen gas were injected into the air and burned. The oxygen concentration of the produced hot gas was kept to similar concentrations as in that of standard air. The hot gas was then accelerated to supersonic speeds at the nozzle section. The test cross section was rectangular, 0.12 m in height, 0.12 m in width, and 0.4 m in length, with a backward-facing step of height 0.01 m and width 0.12 m located 0.075 m from the nozzle exit plane (Fig. 2).

A zirconia (ZrO_2) ceramic coating (0.005 m thick) provided the thermal protection for the metal structure. Optical access was achieved through quartz windows on both sidewalls. The fuel was hydrogen and was injected parallel to the tunnel floor through a fuel-injector slit located along the backward surface of the step at subsonic speed and at room temperature. The equivalence ratio was

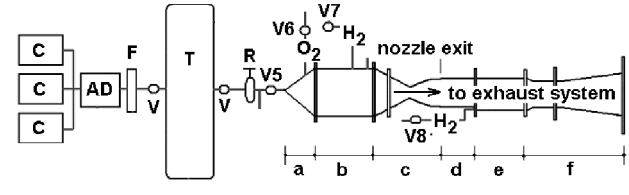

Fig. 1 Schematic of the test facility, where C is the compressor, AD a high-pressure air-dryer, F the filter, V the valves, R the regulator, a the wide angle diffuser and rectifier, b the settling chamber and air heater, c the nozzle section, d the isolator duct, e the supersonic combustor, f the spray-cooled diffuser, and T the air storage tank. (Note: valves V5, V6, V7, and V8 are digitally controlled.)

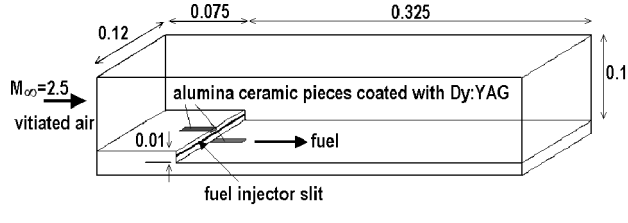

Fig. 2 Schematic of the supersonic combustor. (Note: dimensions in meters.)

set to be about 0.15 at most because more fuel caused a strong precombustion shock system, which caused the main flow to decelerate to subsonic speeds. The injector slit was rectangular, 0.09 m in width with a 0.003-m vertical opening. Because of the low static temperature, ignition was provided by a high-energy spark plug located at a distance of about 0.15 m from the step. Ignition was initiated 2 s after the beginning of the run and 160 μs after reaching steady-state flow rates. Although the flame was held stably at the design point, thermal choke or blowoff can occur just beside the design point. Therefore, an active control system was used to control combustion instabilities and to improve flame holding. The system was based in the design described in Ref. 8. A thick boundary layer develops downstream of the backward-facing step that controls the effective cross-sectional area of the combustor. Four air injectors were installed in the fuel-injection side of the combustor, 0.07 m from the step in a continuous fashion. Air was injected perpendicular to the boundary layer at a subsonic speed to affect the thickness of the boundary layer. Air injection was fixed at 0.5% of the main airflow in mole flow rate. An air injector consisted of 50 holes with diameter of 0.002 m. Air injection was controlled by a system of stop and needle valves operated by four stepping motors. Signals from two pressure transducers on the combustor wall were used as feedback signals for the control. The pressure transducers were installed at 0.03 and 0.06 m downstream of the step. A controller and a personal computer monitored the pressure sensors and controlled the stepping motors according to these signals.

On the fuel-injection side of the combustor, two alumina ceramic pieces of 0.05-m length and 0.01-m width were secured with a high-temperature alumina adhesive along the centerline of the surface inside premachined strips. One of the pieces was placed immediately upstream of the backward step, whereas the other piece was placed immediately downstream of the step (Fig. 2). A steady-state heat transfer analysis was performed to determine the optimum coating thickness.[7] The ceramic pieces were coated with a thin layer ($<$50 μm) of dysprosium YAG thermographic phosphor (equivalent to a coating density of 0.05 kg/m^2), with fluorescence signal uniformity of $\pm$3% and total thickness (alumina ceramic plus phosphor coating) of 0.01 m. The phosphor coating was excited by the 355-nm tripled output of a Nd:YAG laser 1 s after ignition, allowing for establishment of the hydrogen fuel combustion. The emission profile was then recorded at every 1-s time interval within the remaining time of steady-state flow conditions by the use of the system described in Sec. "Laser-Induced-Fluorescence Technique."

Heat-Flux Estimation

Because the surface under consideration did not have time to attain an equilibrium temperature due to the short run time under steady-state flow conditions, transient techniques can be employed to measure heat fluxes. With the transient technique, the measured emission intensity change during testing is used as an indication of the changing surface temperature. By the use of an appropriate theoretical model of the thermal response of the wind-tunnel surface to the heat flux (assumed to be suddenly applied), the latter can be deduced from temperature changes. Such a model should also satisfy the following criteria: 1) The phosphor coating is infinitely thin. 2) The convective heat transfer is transmitted normally into the model surface. 3) The local surface radius of curvature is large. 4) The heat conduction toward the metal nickel structure is negligible, due to the short run time under steady-state conditions ($<$4 s) and the low conductivity of the zirconia and alumina ceramic coatings. Therefore, the one-dimensional unsteady heat conduction equation can be used for both the phosphor layer and the alumina–zirconia ceramic substrate. The thermal model of the surface is shown in Fig. 3. The data reduction model also assumes a surface temperature distribution on the temperature sensitive paint (TSP) layer with both the TSP layer and the substrate material to have a constant temperature T_{ini} at $t = 0$:

$$\frac{\partial \theta}{\partial t} = \alpha \frac{\partial^2 \theta}{\partial y^2} = \frac{\kappa}{\rho c_p} \frac{\partial^2 \theta}{\partial y^2} \tag{1}$$

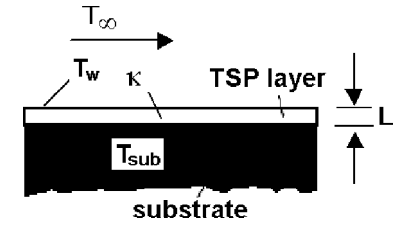

Fig. 3 Thermal model of the surface.

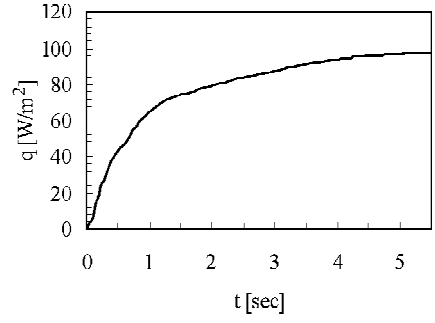

Fig. 4 Transient heat-flux using an assumed time-varying wall temperature distribution.

where, for the TSP layer, $\theta = \theta_{\text{TSP}}(y, t) = T_w - T_{\text{ini}}$ and $\alpha = \alpha_{\text{TSP}}$. For the substrate, $\theta = \theta_{\text{sub}}(y, t) = T_{\text{sub}} - T_{\text{ini}}$ and $\alpha = \alpha_{\text{sub}}$. The boundary conditions are

$$q_w(t) = \kappa_{\text{TSP}} \frac{\partial \theta_{\text{TSP}}}{\partial y}(y = L) = 0, \qquad \theta_{\text{sub}}(y = \infty) = 0$$

The matching conditions on the interface are

$$\theta_{\text{TSP}}(y = 0) = \theta_{\text{sub}}(y = 0)$$

$$\kappa_{\text{TSP}} \frac{\partial \theta_{\text{TSP}}}{\partial y}(y = 0) = \kappa_{\text{sub}} \frac{\partial \theta_{\text{sub}}}{\partial y}(y = 0)$$

Equation (1) was solved numerically by the Crank–Nicholson finite difference scheme, which is second-order accurate and usually stable at large time steps. A validation test for transient heat transfer measurement in a supersonic wind tunnel was performed with an initial temperature of 300 K, a time-varying wall temperature distribution ($T_w - T_{\text{ini}} = 80t^{2/3}$), and the geometry discussed in Sec. "Apparatus and Procedure." The properties of the materials used are given in Ref. 9. The results indicate a steep increase in heat flux value within the first 1.5 s of operation under steady-state conditions, followed by a much smaller increase between the 2.5 and the 4 s of operation of the order of 10% (Fig. 4).

In the present study, the experimentally measured and computationally calculated values of heat flux at 4 s after establishment of steady-state flow rates were compared. (See Sec. "Results and Discussion.") The surface under consideration must continue to behave as though it is semi-infinite in extent throughout the measuring period. (The conductive heat pulse must not reflect off of the back wall of the surface.) The thickness required for semi-infinite behavior is[10] $y^* = 4(\alpha t)^{1/2}$. For typical plastic materials, this depth is approximately 0.004 m for $t = 4$ s; for ceramics it is 0.008 m and for metals it is $\mathcal{O}(0.04)$ m.

The accurate determination of heat flux depends on the degree to which the theoretical model of the thermal response of the wind-tunnel surface to the heat flux satisfies the criteria set out in the beginning of the present section. When all of these factors are taken into account, together with the uncertainties in the nominal wind-tunnel conditions, run time, and operation (described in Sec. "Experimental Apparatus and Procedure"), the overall uncertainty in heat-flux determination is estimated to be typically in the region of $\pm$5%. This measurement compares well with the typical uncertainty of similar

Table 1 Chemical kinetic mechanism of hydrogen–air combustion[2]: rate constant,[a] $k_f = AT^n \exp(-E/RT)$

Reaction	A	E	N
$H_2 + O_2 \leftrightarrow HO_2 + H$	1.0×10^{14}	56000.0	0.0
$H + O_2 \leftrightarrow OH + O$	2.6×10^{14}	16800.0	0.0
$O + H_2 \leftrightarrow OH + H$	1.8×10^{10}	8900.0	1.0
$OH + H_2 \leftrightarrow H + H_2O$	2.2×10^{13}	5150.0	0.0
$OH + OH \leftrightarrow O + H_2O$	6.3×10^{12}	1090.0	0.0
$H + OH + M \leftrightarrow H_2O + M$	2.2×10^{22}	0.0	−2.0
$H + H + M \leftrightarrow H_2 + M$	6.4×10^{17}	0.0	−1.0
$H + O + M \leftrightarrow OH + M$	6.0×10^{16}	0.0	−0.6
$H + O_2 + M \leftrightarrow HO_2 + M$	2.1×10^{15}	−1000.0	0.0
$O + O + M \leftrightarrow O_2 + M$	6.0×10^{17}	−1800.0	0.0
$HO_2 + H \leftrightarrow OH + OH$	1.4×10^{14}	1080.0	0.0
$HO_2 + H \leftrightarrow H_2O + O$	1.0×10^{13}	1080.0	0.0
$HO_2 + O \leftrightarrow O_2 + OH$	1.5×10^{13}	950.0	0.0
$HO_2 + OH \leftrightarrow H_2O + O_2$	8.0×10^{12}	0.0	0.0
$HO_2 + HO_2 \leftrightarrow H_2O_2 + O_2$	2.0×10^{12}	0.0	0.0
$H + H_2O_2 \leftrightarrow H_2 + HO_2$	1.4×10^{12}	3600.0	0.0
$O + H_2O_2 \leftrightarrow OH + HO_2$	1.4×10^{13}	6400.0	0.0
$OH + H_2O_2 \leftrightarrow H_2O + HO_2$	6.1×10^{12}	1430.0	0.0
$H_2O_2 + M \leftrightarrow OH + OH + M$	1.2×10^{17}	45500.0	0.0

[a]Units are cubic centimeters per mole per second.

value in heat-flux estimation made with more conventional transient techniques (thin film or thermocouple gauges).

Computational Fluid Dynamics (CFD) Code

The flowfield inside the supersonic combustor was modeled with a two-dimensional full Navier–Stokes code with a full chemistry model of nine species (i.e., H_2, O_2, O, H, OH, HO_2, H_2O_2, H_2O, and N_2) on a cluster personal computer network arrangement. Nitrogen was inert. The chemical kinetic mechanism of hydrogen–air combustion was given by 19 elementary reactions[2] (Table 1), where M is the third body that absorbs excess energy release during the collision process. To avoid error accumulation over a specific species, the total mass conservation equation and single species conservation equations were solved simultaneously. Hence, the governing equations in the conservation form are as follows:

$$\frac{\partial U}{\partial t} + \frac{\partial F}{\partial x} + \frac{\partial G}{\partial y} = \frac{\partial F_v}{\partial x} + \frac{\partial G_v}{\partial y} + S \tag{2}$$

where U is the conservative vector, F and G are the convective terms, F_v and G_v are the viscous terms, and S is the chemical reaction source term:

$$U = \begin{pmatrix} \rho \\ \rho u \\ \rho v \\ E \\ \rho_i \end{pmatrix}, \qquad F = \begin{pmatrix} \rho u \\ \rho u^2 + p \\ \rho u v \\ (E + P)u \\ \rho_i u \end{pmatrix}$$

$$G = \begin{pmatrix} \rho v \\ \rho u v \\ \rho v^2 + P \\ (E + P)v \\ \rho_i v \end{pmatrix}, \qquad F_v = \begin{pmatrix} 0 \\ \sigma_x \\ \tau_{xy} \\ \sigma_x u + \tau_{yx} v + q_x \\ -\dot{m}_{ix} \end{pmatrix}$$

$$G_v = \begin{pmatrix} 0 \\ \tau_{yx} \\ \sigma_y \\ \tau_{xy} u + \sigma_y v + q_y \\ -\dot{m}_{iy} \end{pmatrix}, \qquad S = \begin{pmatrix} 0 \\ 0 \\ 0 \\ 0 \\ \dot{\omega}_i \end{pmatrix} \tag{3}$$

where

$$P = \sum_{i=1}^{NS} \rho_i \frac{R}{W_i} T, \qquad E = \sum_{i=1}^{NS} \rho_i c_{pi} T - \sum_{i=1}^{NS} \rho_i \frac{R}{W_i} T + \frac{\rho}{2}(u^2 + v^2)$$

$$\sigma_x = \lambda\left(\frac{\partial u}{\partial x} + \frac{\partial v}{\partial y}\right) + 2\mu\left(\frac{\partial u}{\partial x}\right)$$

$$\sigma_y = \lambda\left(\frac{\partial u}{\partial x} + \frac{\partial v}{\partial y}\right) + 2\mu\left(\frac{\partial v}{\partial x}\right)$$

$$\tau_{xy} = \tau_{yx} = \mu\left(\frac{\partial u}{\partial y} + \frac{\partial v}{\partial x}\right), \qquad q_x = -\kappa\frac{\partial T}{\partial x} - \rho\sum_{i=1}^{NS} D_{im} h_i \frac{\partial Y_i}{\partial x}$$

$$q_y = -\kappa\frac{\partial T}{\partial y} - \rho\sum_{i=1}^{NS} D_{im} h_i \frac{\partial Y_i}{\partial y}, \qquad \dot{m}_{ix} = -\rho D_{im}\frac{\partial Y_i}{\partial x}$$

$$\dot{m}_{iy} = -\rho D_{im}\frac{\partial Y_i}{\partial y}, \qquad \lambda = -\frac{2}{3}\mu, \qquad \mu = \mu_\ell + \mu_t$$

$$\kappa = \kappa_\ell + \kappa_t, \qquad D_{\mathrm{im}} = D_{\mathrm{im}\ell} + D_{it}$$

The values of c_{pi}, h_i, and s_i were considered as polynomials of temperature, and the equation of state for ideal gases was used. The coefficients of the polynomials were determined from the polynomial curve fitting developed in Ref. 11. Body forces, bulk viscosity, Soret effect, Dufour effect, and diffusion due to pressure gradient were neglected. The transport properties, the viscosity coefficient, and the thermal conductivity of each species were determined from Sutherland's formulas (see Ref. 12). The mixture viscosity and thermal conductivity were determined from Wilke's formula and Wassiljewa's equation, respectively (see Ref. 12). The effective and binary diffusion coefficients were obtained from Chapman–Cowling and Chapman–Enskog formulas (see Ref. 12). The Baldwin–Lomax algebraic turbulence model was employed to provide a turbulent contribution to the viscosity.[13] It has been shown in Refs. 5 and 14 that this turbulence model can successfully calculate separated flows with much more complicated grid geometry than that of the present study. The values of the turbulent thermal conductivity of the mixture and turbulent diffusion coefficient of ith species were obtained from the eddy-viscosity coefficient by the assumption of constant turbulent Prandtl and Lewis numbers equal to 0.91 and 1.0, respectively. They can be expressed as follows:

$$\kappa_t = \mu_t c_p / 0.91, \qquad D_{it} = 1.0\kappa_t / \rho c_p \tag{4}$$

The system of the governing equations has been solved with an explicit Harten–Yee non-MUSCL modified-flux type total variation diminishing (TVD) scheme (see Ref. 15) accurate in time and space. The two-dimensional, rectangular physical coordinate system (x, y) was transformed into the computational coordinate system (ξ, η) to solve the problem on a uniform grid. The Roe's average Riemann solver was used (see Ref. 15) due to its simplicity and its ability to return to the exact solution whenever the variables lie on a shock or contact discontinuity. The Courant–Friedrichs–Lewy (CFL) number was chosen as 0.7 to obtain rapid convergence and to avoid unsteadiness in calculation.

The numerical diffusion has been checked with different kinds of limiters in a TVD scheme on a simulation study of the physics of mixing and combustion with the present code. The study indicated a significant reduction of the numerical diffusion when a change of the limiter in the TVD scheme from minmod to "superbee" was made. No significant difference in the pattern of shocks and their positions was found between the two limiters, and, for both cases, similar tendencies of pressure distributions existed all over the flowfields. However, the significant difference in hydrogen penetration distance led the author to perform the simulation using the superbee limiter because it can reduce the numerical diffusion in the present solution of a mixing problem.

The study indicated that the inclusion of the turbulence model causes an increase in the viscosity, the diffusion coefficient, and the thermal conductivity, which causes an increase in the size of the recirculation region and boundary-layer thickness both upstream and downstream of the injector. Downstream of the injector, the turbulence model causes higher penetration and mixing of hydrogen due to the enhancement of the diffusion coefficient. The code has been validated with the experimental data of Ref. 16. The code was considered suitable for calculating the induced flowfield by hydrogen injection in a supersonic flow.

Computational Domain and Boundary Conditions

The geometry of the grid used for the numerical study is the same as that of the model combustor used in the experiments. (See Sec. "Apparatus and Procedure.") The grid was generated using a two-dimensional transfinite interpolation technique[17]: 1) generation of the one-dimensional line grids at all junctions of the domain surfaces with high density at all walls and in the region of the step where high gradients exist, to ensure the accuracy of the simulations and 2) generation of the two-dimensional surface grids for all of the domain boundary surfaces by the use of the one-dimensional line grids as the interpolation boundaries and the application of any geometric constraints.

The sensitivity of the numerical solution to the computational grid was checked with five grid densities and distributions. Smoothing and stabilizing parameters were kept to a minimum during the grid-sensitivity studies. The grid was refined in each direction of the two dimensions while the other dimension was held fixed. The study showed a difference of less than 1% between results for grid systems of more than 350 nodes in the longitudinal direction and 80 nodes in the vertical direction. A grid system of 400×90 nodes was selected for these simulations. The minimum grid spacing was 10 μm (in the neighborhood of the wall). The boundary conditions at the top and bottom walls were no-slip and adiabatic, $(\partial T/\partial n)_w = 0$. For noncatalytic walls, the normal derivative of species mass fraction also vanishes, and, consequently, the gradient of total density becomes zero. The temperature, pressure, and density at the inflow boundary were assumed steady. At the outflow boundary, the variables were determined by first-order extrapolation if the flow was supersonic in character or by zero-order extrapolation when the flow was subsonic. The velocity profile of the airflow at the entrance was assumed uniform. In the computational study, the main airflow was dry air, whereas in the experiments it was vitiated air (containing water and radicals).

The boundary condition at the fuel-injector exit was uniform condition, and its static pressure was made equal to that of the surrounding mainflow. Therefore, the fuel velocity varied according to the equivalence ratio (ER) and the pressure at the exit of the fuel injector. For $T_o = 800$ K and ER $= 0.15$, the fuel velocity was 335 m/s ($M = 0.25$). After ignition and flame establishment at the step, the fuel velocity decreased to 215 m/s ($M = 0.19$), due to an increase of the ambient pressure. In the simulations, ignition was initiated first by calculation of a steady-state solution (freezing all chemical reactions) and then by provision of a supply of ignition energy at $x = 0.15$ m from the step for 40 μs (that used to generate a shock wave). The total energy supplied was about 9.5 J. The flame began to propagate upstream with the shock wave after it. The solution history was monitored and the steady-state solution was selected if the change of the flowfield parameters residuals became small or the maximum number of iterations was satisfied. The convergence criterion required that the residuals be smaller than 10^{-5} for the mass, momentum, and energy equations.

Results and Discussion

A precombustion shock is generated near the step, and the average pressure level in the combustor is high (Fig. 5a). A separation region is observed behind the step (Fig. 5b). Hydrogen spreads both upstream and downstream of the injector due to stretching and folding of the fluid layers. It is then transported toward the core of the main airflow, creating a shear layer (Figs. 5b and 5c). Because of interaction between the main and injecting flows, air enters the recirculation region downstream the backward-facing step, and it mixes with hydrogen. When this hydrogen–air mixture reaches the top of the recirculation region, it mixes further with air. This enhanced hydrogen–air mixture is carried downstream by the main flow, and mixes with more air and spreads by expansion and diffusion phenomena. Because, around the injector, there is a high mass concentration of hydrogen, mixing is caused by both diffusion and convection of hydrogen. Further downstream, in the recirculation region, mixing is mainly due to diffusion. The reacting region is located in this shear layer, precisely where the temperature and pressure recover due to the shock wave, which favors combustion (Figs. 5a, 5d, and 5e). The activation of the diffusion terms in the species continuity equations of the governing equation (2) enhances mixing, which causes a larger penetration of hydrogen into the flow. Because the dynamic pressure of the fuel is low due to the low ER, it is conjectured that separation has a large effect on the fuel flow.

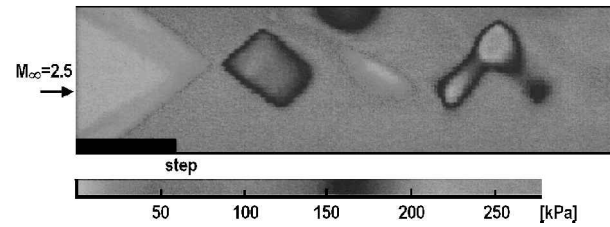

a) Pressure distribution

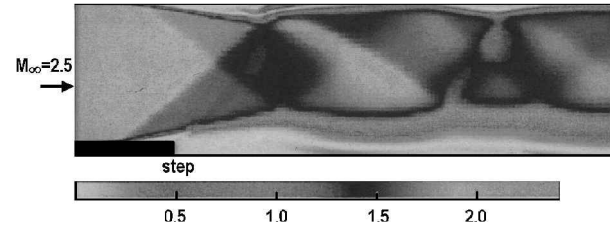

b) Mach number distribution

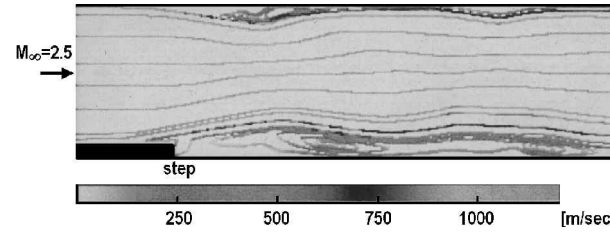

c) Velocity contours and streamlines

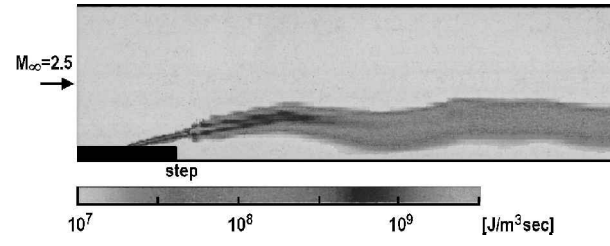

d) Heat release distribution

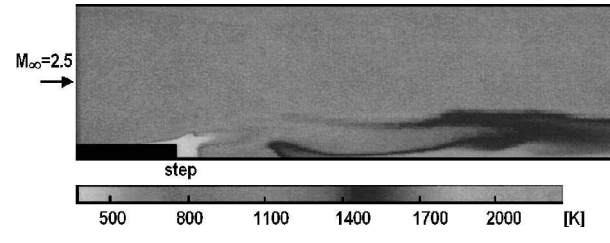

e) Temperature distribution

Fig. 5 Typical flow property distributions inside the supersonic combustor.

It is believed that the mixing efficiency is higher than that under cold flow conditions because of the vortex structure generated in the separation region. Under the present conditions, the shock wave is supported by the high backpressure due to combustion, which, in turn, induces separation that transports fuel and creates a favorable reaction. The whole flowfield is not changed into subsonic, and the main flow still remains supersonic (Fig. 5b). The proposed flowfield inside the combustor is depicted in Fig. 6.

Figure 7 shows the water production zone in the reacting flow region. The highest mole fraction of water appears at about the middle of the combustible mixing layer, where a stoichiometric mixture is present. The upper region of the highest water mole fraction layer is fuel lean. The lower region is fuel rich. It is conjectured that the rise in temperature and pressure due to chemical reaction expands the recirculation zone, resulting in a change in the location and steepness of the separation shock wave in comparison with nonreacting case.

The surface temperature rise deduced from the measured emission intensities of the phosphor and calculated from the CFD code were used to estimate the heat flux to the surface. The thermal model of the unsteady heat conduction process described in Sec. "Heat-Flux Estimation" was used for this purpose. The comparison is depicted in Fig. 8. Good agreement on the regions with lower heating can be observed, although in areas with intense combustion, the CFD predictions are poor, with the experimental study indicating substantially higher heating rates. The disagreement is believed to be due mainly to the inability of the code to take into account the effect of the wall and its complicated contribution to the chemistry of the combustion, for example, heterogeneous reactions occurring at the interfaces of the gas–solid wall interface. In the present case, the surface acts as a catalyst for the gas reactions, for example, catalytic surface recombination of dissociated diatomic atoms, which are known to be first-order reactions. Another reason for the disagreement is the three-dimensional nature of the combustion, which is not modeled in the present study (two-dimensional model was assumed), due to the huge computational effort required.

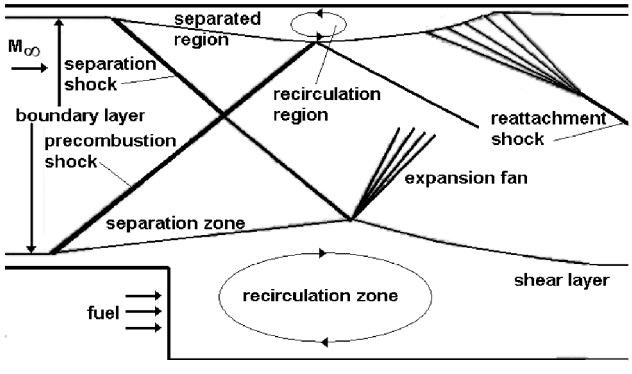

Fig. 6 Proposed flowfield inside the combustor.

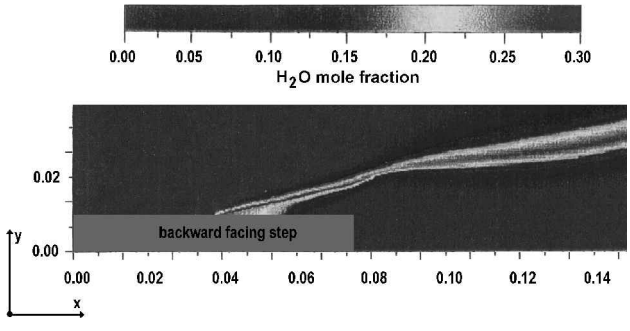

Fig. 7 Water (H_2O) mole fraction in fully developed chemically reacting flowfield. (Note: all dimensions in meters.)

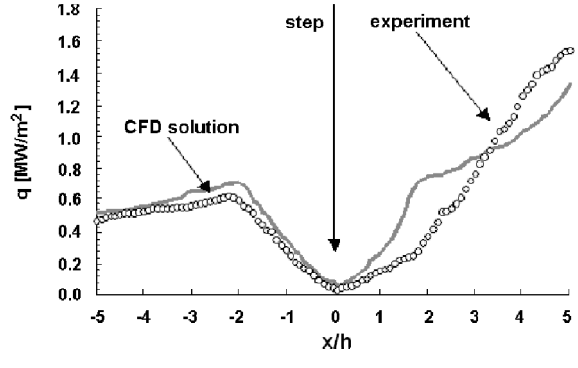

Fig. 8 Heat flux comparisons along the centerline on the fuel injection side.

Conclusions

This study is one of the first to use LIF surface thermometry for high-temperature measurements on a model supersonic combustor. Though it is necessary to apply a thin phosphor coating to the surface on which temperature measurements are to be conducted, the thermal resistance of the coating is negligible. With respect to the spatial resolution capability of LIF thermal imaging, the only theoretical limitation is the precision of available optics. In practice, however, the resolution will be a function of the surface area to be measured, which determines the level of optical magnification, as well as the quality of the phosphor surface. Coupled with full Navier–Stokes simulations, the result is a methodology that quickly provides a wealth of information critical to the design of thermal protection systems for applications involving engine design, reentry vehicles, missiles, and supersonic transports.

References

[1]Billig, F. S., "Supersonic Combustion Ramjet Missile," *Journal of Propulsion and Power*, Vol. 11, No. 6, 1995, pp. 1139–1146.

[2]Jachimowski, C. J., "An Analytical Study of the Hydrogen–Air Reaction Mechanism with Application to Scramjet Combustion," NASA TP-2791, May 1988.

[3]Donohue, J. M., and McDaniel, J. C., "Complete Three-Dimensional Multiparameter Mapping of a Supersonic Ramp Fuel Injector Flowfield," *AIAA Journal*, Vol. 34, No. 3, 1996, pp. 455–462.

[4]Kontis, K., and Stollery, J. L., "Control Effectiveness of a Jet–Slender Body Combination at Hypersonic Speeds," *Journal of Spacecraft and Rockets*, Vol. 34, No. 6, 1997, pp. 762–768.

[5]Gruber, M. R., and Goss, L. P., "Surface Pressure Measurements in Supersonic Transverse Injection Flowfields," *Journal of Propulsion and Power*, Vol. 15, No. 5, 1999, pp. 633–641.

[6]Kanda, T., Saito, T., Kudo, K., Komuro, T., and Ono, F., "Mach 6 Testing of a Scramjet Engine Model," AIAA Paper 96-0380, Jan. 1996.

[7]Kontis, K., Syogenji, Y., and Yoshikawa, N., "Surface Thermography by Laser-Induced Fluorescence of Dy:YAG," *Aeronautical Journal*, Vol. 106, No. 1062, 2002, pp. 453–457.

[8]Takahashi, S., Sato, N., Tsue, M., Kono, M., Nakamura, M., Kondo, H., and Ujiie, Y., "Control of Flame Holding in Supersonic Airflow by Secondary Air Injection," *Journal of Propulsion and Power*, Vol. 14, No. 1, 1998, pp. 18–23.

[9]Munz, D., and Fett, T., *Ceramics: Mechanical Properties, Failure Behavior, Materials Selection*, Springer-Verlag, New York, 1999, pp. 47–61.

[10]Schultz, D. L., and Jones, T. V., "Heat Transfer Measurements in Short-Duration Hypersonic Facilities," AGARD-AG-165, Feb. 1973, pp. 6–37.

[11]Moss, J. N., "Reacting Viscous-Shock-Layer Solutions with Diffusion and Mass Injection," NASA TR-411, June 1974.

[12]Reid, R. C., Prausnitz, J. M., and Poling, B. E., *The Properties of Gases and Liquids*, McGraw–Hill, New York, 1988, pp. 112–192.

[13]Baldwin, B. S., and Lomax, H., "Thin Layer Approximation and Algebraic Model for Separated Turbulent Flows," AIAA Paper 78-0257, Jan. 1978.

[14]Kontis, K., Qin, N., Stollery, J. L., and Edwards, J. A., "Hypersonic Performance of a Lifting Elliptic Cone with and without Strakes," *Journal of Spacecraft and Rockets*, Vol. 37, No. 1, 2000, pp. 21–27.

[15]Yee, H. C., "A Class of High Resolution Explicit and Implicit Shock Capturing Methods," NASA TM-101088, Oct. 1989.

[16]Kraemer, G. O., and Tiwari, S. N., "Interaction of Two-Dimensional Transverse Jet with a Supersonic Mainstream," NASA CR 175446, May 1983.

[17]Eiseman, P. R., "Grid Generation for Fluid Mechanics Computation," *Annual Review of Fluid Mechanics*, Vol. 17, Feb. 1985, pp. 487–522.